Published in final edited form as:
Microsc Microanal. 2013 August ; 19(4): 791–798. doi:10.1017/S1431927613001530.

Endoscopic Fluorescence Lifetime Imaging for *In Vivo* Intraoperative Diagnosis of Oral Carcinoma

Yinghua Sun[1], **Jennifer E. Phipps**[1], **Jeremy Meier**[2], **Nisa Hatami**[1], **Brian Poirier**[3], **Daniel S. Elson**[4], **D. Gregory Farwell**[2], and **Laura Marcu**[1,*]

[1]Department of Biomedical Engineering, University of California, Davis, CA 95616, USA

[2]Department of Otolaryngology-Head and Neck Surgery, University of California Davis, Sacramento, CA 95817, USA

[3]Department of Pathology, University of California Davis, Sacramento, CA 95817, USA

[4]Department of Surgery, Hamlyn Centre, Imperial College London, London SW7 2AZ, UK

Abstract

A clinically compatible fluorescence lifetime imaging microscopy (FLIM) system was developed. The system was applied to intraoperative *in vivo* imaging of head and neck squamous cell carcinoma (HNSCC). The endoscopic FLIM prototype integrates a gated (down to 0.2 ns) intensifier imaging system and a fiber-bundle endoscope (0.5-mm-diameter, 10,000 fibers with a gradient index lens objective 0.5 NA, 4-mm field of view), which provides intraoperative access to the surgical field. Tissue autofluorescence was induced by a pulsed laser (337 nm, 700 ps pulse width) and collected in the 460 ± 25 nm spectral band. FLIM experiments were conducted at 26 anatomic sites in ten patients during head and neck cancer surgery. HNSCC exhibited a weaker florescence intensity (~50% less) when compared with healthy tissue and a shorter average lifetime (τ_{HNSCC} = 1.21 ± 0.04 ns) than the surrounding normal tissue (τ_N = 1.49 ± 0.06 ns). This work demonstrates the potential of FLIM for label-free head and neck tumor demarcation during intraoperative surgical procedures.

Keywords

fluorescence lifetime imaging microscopy (FLIM); tissue autofluorescence; endoscopy; head and neck squamous cell carcinoma (HNSCC); cancer diagnosis; intraoperative diagnosis

Introduction

Tissue autofluorescence has been explored for noninvasive disease diagnosis owing to the clinical need for real-time diagnostic techniques without the use of excisional biopsy (Andersson-Engels et al., 1990; Richards-Kortum et al., 1994; Ramanujam, 2000). Fluorescence lifetime imaging microscopy (FLIM) is one promising imaging modality that can demarcate malignant from normal tissue by extracting multiple indicative parameters

*Corresponding author. lmarcu@ucdavis.edu.

from autofluorescence signals including intensity, lifetime, and wavelength (Andersson-Engels et al., 1993; Cubeddu et al., 2002; Elson et al., 2004). This method is particularly appropriate for intraoperative application because the time-resolved images are minimally affected by artifacts caused by irregular tissue surface, nonuniform illumination, or presence of endogenous absorbers such as blood (Elson et al., 2004). Whereas these factors may substantially affect the signal and subsequently the diagnostic capability for intensity-based diagnosis techniques, the inherent ratiometric nature of lifetime measurements provides increased robustness. Fluorescence lifetime measurements are able to complement intensity and spectral measurements, providing additional information to characterize the chemical composition, metabolism, and environmental factors of living tissue and biological samples (Cubeddu et al., 2002; Elson et al., 2004; Marcu, 2012). Therefore, FLIM has inherent advantages for quantitative analysis of biological tissues *in vivo*.

In this work, a compact clinically compatible FLIM system was developed for intraoperative cancer diagnosis. In collaboration with head and neck surgeons, this apparatus was designed and built to accommodate specific clinical requirements including use of a semiflexible probe for remote access to patients, sterilizability of the imaging probes, system mobility between operating rooms, and compliance with medical safety regulations. The critical performance of this FLIM system relied on the use of two key optical components—a high temporal resolution image intensifier system and a flexible fiber image guide. Before the clinical testing, this system was evaluated using standard fluorophores and animal models *in vivo* (Sun et al., 2009; Phipps et al., 2011). More detailed information on the system development was reported previously (Elson et al., 2007; Sun et al., 2009).

This study evaluates the potential of endoscopic FLIM to accurately diagnose lesions intraoperatively in patients presenting with head and neck squamous cell carcinoma (HNSCC). HNSCC is a common cancer, affecting over 40,000 people each year in the US alone.[a] Surgical resection is the standard treatment for HNSCC followed by concurrent or sequential chemoradiotherapy. However, frequently these tumors are challenging to surgically resect because of the subtle interface at the margin between normal and abnormal tissue. This determination is critical as overly aggressive surgical resection can result in reduced function (swallowing/speech) and under-resection will predispose to tumor recurrence and potential increased morbidity or even mortality. Intraoperative determination of an adequate surgical margin is typically done by visual inspection and palpation. FLIM can be used in the analysis of tissue autofluorescence and therefore has the inherent potential to provide rapid feedback on the molecular changes associated with HNSCC and aid in the identification of surgical resection margins.

Methods

FLIM Endoscope Probe and Instrumentation

FLIM techniques can be categorized into time-domain or frequency-domain, and wide-field imaging or scanning, according to the types of light sources and detectors used. Wide-field imaging time-domain FLIM is currently the most widely used modality for *in vivo* or

[a]National Cancer Institute 2012 (http://www.cancer.gov/cancertopics/types/oral).

clinical application because of its relative robustness and fast imaging speed. In this work, we built a portable time-domain wide-field FLIM apparatus that was coupled with a fiber image guide endoscopic probe. The apparatus schematic is shown in Figure 1. The gated optically intensified CCD camera (ICCD, 4 Picos, Stanford Computer Optics, Berkeley, CA, USA) had a minimum gating time of 200 ps and a repetition rate up to 200 kHz. Tissue autofluorescence was induced by a fiber-delivered 337 nm pulsed nitrogen laser (MNL 205, LTB Lasertechnik, Berlin, Germany) with 700 ps pulse width and ≤50 Hz repetition rate.

A fully integrated semiflexible fiber optic endoscope probe was built for fluorescence lifetime imaging application *in vivo*, as shown in Figure 1b. This included an optical delivery fiber (600 μm, NA 0.48, Thorlabs, Newton, NJ, USA) and a 1.7-m-long, 0.6-mm-diameter 10,000 fiber image guide with a gradient index lens termination to image the fluorescence emission (4-mm working distance, 4-mm-diameter field of view). The total length was 3 m, and it consisted of three parts: a 2.4-mm-diameter, 16-mm-long hollow stainless steel rigid tip; a 1-m-long common part integrating the fiber image guide and optical delivery fiber; and a bifurcation into two legs. The light delivery fiber was optically aligned and cemented solidly to the fiber image guide within the stainless steel tube, which was sufficiently robust to allow operators to hold and point the endoscope to specific tissue regions of interest as indicated in Figure 1c. The common part of the probe had an outer diameter of 5 mm and a minimum bending radius of 10 cm, similar to that of the fiber image guide, and was contained within a coiled stainless steel furcation tube. After bifurcation, the optical fiber and fiber image guide were protected in a tube including a PVC jacket (3.8-mm outer diameter) and an inner tube (1-mm inner diameter), and were terminated with SMA connectors. The laser delivery fiber was longer than the fiber image guide to allow a higher freedom of movement during the *in vivo* work.

A 20× microscope objective and 150-mm focal length doublet lens were used to magnify the proximal facet of the fiber image guide onto the ICCD chip. A filter wheel was inserted into the optical path to select up to six emission filters. Only one bandpass filter was used throughout this study: 460 ± 25 nm (central wavelength ± bandwidth). Signal synchronization was optimized for both the ICCD and the pulsed laser using the CCD camera as the master trigger at 30 Hz. This triggered the nitrogen laser, which in turn triggered the short intensifier gate. The precise delay between the gating time and the fluorescence signal was controlled by an internal delay generator that had a resolution of 10 ps. The electronic trigger of the laser had a jitter of less than 200 ps. The temporal gate width of the 4 Picos was varied from 0.2 to 1 ns depending on the signal level found for each experiment.

The frame rate of the CCD camera was 30 Hz at the resolution of 480 × 736 pixels. For most tissue samples, one intensity gated image required the integration of 128 laser excitation pulses in order to obtain sufficient signal to noise. Data acquisition times for each measurement were ~2 min including one steady-state image and a series of up to 29 time-gated images (0.5 ns gate time, 0.5 ns relative delay time step). The camera “4 SPEC” software controlling the gated optical intensifier was customized for FLIM image acquisition. The overall system performance test followed procedures similar to those previously reported by our group (Elson et al., 2007; Sun et al., 2009).

To bring FLIM into the operating room for tumor demarcation *in vivo* on human subjects, the system was designed to meet specific clinical requirements, and the FLIM probe was integrated and mounted on a mobile cart. The process for acquiring measurements of *in vivo* tissue autofluorescence is demonstrated in Figure 1c, showing the endoscope held in the oral cavity by a surgeon.

Clinical Validation in Human Subjects

Ten patients with suspected HNSCC were included for FLIM measurement and a total of 26 sites were examined. The study was approved by the Institutional Review Board at the University of California at Davis and all patients involved in this research were consented for the study. The FLIM instrument was placed on a mobile cart so that it could be easily transferred between operating rooms before the experiment. Before data collection from a patient, the rigid distal end of the endoscopic probe was placed in a PMMA protective tube that could be sterilized and sealed with a sapphire window. This tube extended beyond the end of the probe and acted as a spacer between the probe and the tissue in order to maintain the 4-mm working distance of the probe. For intraoperative measurement, the protective sterile tube was gently positioned perpendicular to the interrogated tissue surface. After the measurement was completed, tissue biopsies were taken from the measured region and histopathological analysis was independently conducted by a clinical pathologist. The energy density delivered at the tissue surface was 0.16 mJ/cm^2 per pulse. This was 20 times lower than the skin maximum permissible exposure value of 3.2 mJ/cm^2 for UV lasers according to the American National Standard for Safe Use of Lasers.

Image and Data Processing

Image processing and lifetime deconvolution were conducted using a custom-built graphical user interface written using MATLAB. A rapid deconvolution was achieved through the polynomial Laguerre expansion, which allowed the fluorescence impulse response function, the fluorescence lifetime, the integrated intensity, and the Laguerre coefficients (LECs) to be calculated (Jo et al., 2006). The Laguerre technique is based on a nonparametric model that allows the evaluation of fluorescence decays from complex fluorescent systems such as biological tissues without *a priori* assumptions about the decay function or number of fluorescent molecular species within the fluorescent system (Liu et al., 2012). In addition, the Laguerre functions contain a built-in exponential term and are orthogonal, which results in a fast, convenient, unique, and complete expansion of the exponential decays, and in addition produces an additional set of decay parameters (i.e., LECs) for enhanced analysis of the fluorescence decay features. In this work, up to four Laguerre polynomials were used in the expansion to the fluorescence impulse response profile for each measurement based on linear least-square error, resulting in a set of four LECs. The parameter α found within the Laguerre polynomials was fixed at 0.8 based on the Kernel memory length and the number of Laguerre functions, allowing for the functions to decay sufficiently close to zero by the end of the fluorescence decay (Jo et al., 2006). The resulting function could then be used to calculate the integrated intensity and the average fluorescence lifetime by computing the interpolated time at which the intensity falls to $1/e$ of the initial intensity. The tissue FLIM images (480 × 736 pixels) presented in this paper took less than 60 s to process using an

algorithm that was implemented on a PC with an Intel Core 2 CPU 6600 at 2.40 GHz and 1 GB RAM.

Results

FLIM System Performance Test

Before *in vivo* application, the FLIM instrument was evaluated and tested using a standard target, various fluorophores, and biomolecules. Figures 2a and 2b demonstrate the steady-state (intensity) image of three fluorophores and the FLIM system's ability to resolve these samples based on their fluorescence lifetimes. Two dye solutions, coumarin 120 (C120) and 9-cyanoanthracene (9CA) in ethanol, were loaded into capillary tubes and placed on top of a bed of dry collagen fibers (Collagen type I from bovine achilles, Sigma-Aldrich, St. Louis, MO, USA). Collagen is an important tissue fluorophore present in all epithelial tissues including HNSCC (Pavlova et al., 2009; Schwarz et al., 2009). These three fluorescent samples had overlapping emission spectra and were all detectable in the 460/50 nm bandpass filter, as seen in Figure 2a, yielding no distinction between the fluorescence signals. However, the contrasting fluorescence lifetimes provided a way to demarcate these three fluorophores as shown in Figures 2b and 2c. The average lifetime values (Fig. 2d) were (mean ± full-width at half-maximum) C120: 3.9 ± 0.1 ns, 9CA: 10.3 ± 0.8 ns, and collagen I: 5.0 ± 0.6 ns, consistent with those reported in the literature (Richards-Kortum & Sevick-Muraca, 1996; Lakowicz, 2006). The temporal instrument response function was evaluated as 0.5 ns using a short-lifetime dye, rose bengal, in methanol. In addition, the system spatial resolution was tested using a standard 1951 USAF resolution test chart and was found to be at least 35 μm, sufficient for many tissue diagnosis applications. This was fundamentally limited by the diameter and pitch of the optical fibers within the fiber image guide. The zoomed image (inset) in Figure 2c clearly shows the visible individual fibers. In the current design, the image bundle included 10,000 optical fibers and the spatial resolution could be improved by increasing the number of fibers within the image bundle.

Endoscopic Imaging of Tissue Autofluorescence: Intensity and Lifetime

The custom-made semiflexible fiber optic endoscope probe provided very good access to tumors in the oral cavity at the time of the surgery. The investigated tissues were grouped into four types based on their location: buccal mucosa, tongue, palate, and floor of the mouth. Figure 3 demonstrates one representative group of fluorescence intensity and lifetime images, which were collected from buccal mucosa. Evaluation of the normal mucosa (Figs. 3a, 3e) was based on a measurement taken from a distal area identified as normal by the surgeon. Measurements taken from tumor areas were classified by histopathology as carcinoma *in situ* (Figs. 3b, 3f), and tumor margin with surrounding normal tissue (Figs. 3c, 3g). Their corresponding intensity and lifetime histograms are displayed in Figures 3d and 3h. The intensity values from these three images were I_{normal} = 3,646 ±1,979 AU (±standard deviation), I_{margin} = 2,003 ± 1,038, and I_{HNSCC} = 783 ±416. The intensity value was estimated based on the pixel intensity value after background subtraction, which removed the baseline of 20,000 from the raw data. The lifetime values were $\hat{o}_{\text{normal}}$ = 1.39 ± 0.11 ns, $\hat{o}_{\text{margin}}$ = 1.14 ±0.10 ns, and $\hat{o}_{\text{HNSCC}}$ = 1.07 ±0.09 ns for these three representative images. The HNSCC exhibited a weak fluorescence emission and short

lifetime compared with the normal tissue, whereas the marginal area displayed a transitional fluorescence lifetime and intensity. To extract the quantitative information, intensity and lifetime histograms were plotted in Figures 3d and 3h, which demonstrated three partially resolved distributions from normal, tumor, and margin, respectively. The profile of cancerous tissue displayed a left skew in contrast to the normal tissue, implying a decrease in fluorescence lifetime and intensity for the tumor region.

Statistical Analysis

Statistical analysis was conducted for all 26 sites to investigate the differentiation of HNSCC and the surrounding normal tissue for different parameters including the average fluorescence intensity, lifetime, and LECs values found from each image field. The main results are summarized in Table 1, including the mean values and standard errors for each parameter for normal and tumor samples (13 for normal and 13 for tumor). At the bottom of the table, the *p*-value between the two groups is listed to evaluate the significance. The overall average lifetime in tumor tissue decreased by 18.9% from the normal tissue value $\tau_{\text{normal}} = 1.49 \pm 0.06$ ns to $\tau_{\text{tumor}} = 1.21 \pm 0.04$ ns. The statistical difference was significant based on the *p*-value of 0.0009. In addition, the average intensity decreased clearly in the tumor tissue, showing a 47.8% drop compared with normal tissue, but the *p*-value was slightly higher at 0.012.

One-way analysis of variance (ANOVA) was applied to the statistical analysis of fluorescence lifetimes and intensities. Figures 4a and 4b are ANOVA box plots showing the difference of means, standard deviations, and distribution of lifetimes and intensities between normal and tumor, respectively. The fluorescence lifetimes of tumor and normal groups demonstrated an obvious separation with a low *p*-value <0.001, whereas the standard deviation of intensities in normal tissue is larger with a *p*-value < 0.05. To test the differentiation between tumor and normal tissue, a scatter plot of lifetime versus intensity was also plotted in Figure 5a. Most of the tumor data points are located toward the bottom left region because of their low value in both intensity and lifetime, whereas the normal group is mainly distributed toward the upper right region because of their high emission intensities and long lifetimes. A boundary can be drawn to separate these two groups with only a few points incorrectly classified (sensitivity 87%, specificity 87%). Furthermore, we analyzed the additional parameters retrieved from the fluorescence signal in the form of the LECs (Jo et al., 2006). Here, the LECs were named as LEC-0, LEC-1, LEC-2, and LEC-3. These LEC values were treated as additional parameters to differentiate HNSCC from normal tissue, as presented in Table 1. Among the four coefficients, LEC-1 had the lowest *p*-value of 0.008 and a scatter plot of LEC-1 and lifetime was used to demonstrate the distribution of tumor and normal samples. A slight improvement for the differentiation of tumor and normal tissue was displayed in this plot, as seen in Figure 5b (sensitivity 87%, specificity 100%). Consequently, LEC-1 can be used as a potential parameter to optimize the diagnostic accuracy of carcinoma. This method has also been exploited in our previous work using large data sets for the study of atherosclerosis (Marcu et al., 2009).

Discussion

This paper presents the first use of endoscopic FLIM for HNSSC demarcation in a clinical setting, and is particularly focused on the *in vivo* intraoperative diagnosis in patients. Results have demonstrated the potential to noninvasively differentiate tumor and normal tissue by analyzing autofluorescence within the 460 ± 25 nm wavelength band previously demonstrated to correspond to the NAD(P)H fluorescence emission (Lakowicz, 2006; Pavlova et al., 2009; Schwarz et al., 2009). Both the intensity and the fluorescence decay characteristics of the fluorescence emission (average lifetime and LECs) were able to discriminate tumor from normal areas. The decrease in intensity and lifetime is consistent with previous reports on the study of head and neck tumor (Skala et al., 2007; Schwarz et al., 2009). It has been found that the autofluorescence of oral mucosa upon UV excitation originates primarily from collagen and NADH (Skala et al., 2007; Schwarz et al., 2009). In our study, the fluorescence signal was collected through a relatively broad bandwidth 460/50 nm filter, which should record a combination of collagen and NADH emission signals. On the basis of the previous results and new results from this study, this sub-band appears to be appropriate for carcinoma diagnosis because it provides a reasonable intensity signal, as well as a significant lifetime contrast between cancerous and normal tissue (Sun et al., 2009). In the normal oral tissue, autofluorescence mainly originates from the extracellular matrix proteins in tissue, in particular collagen fiber, which has a bright broadband emission (under UV excitation) from 380 to 500 nm and a long lifetime in the range of 2.5–5 ns. It has been widely reported that there is destruction of structural protein in tissue concurrent with the spread of malignant cells during the progression of carcinoma (De Veld et al., 2005; Skala et al., 2007; Schwarz et al., 2009). In oral carcinoma, it has also been reported that the main contributor to the fluorescence emission is NADH, a co-enzyme associated with cellular metabolism (De Veld et al., 2005; Skala et al., 2007; Schwarz et al., 2009). During the disease progression from healthy to malignant, the contribution of NADH fluorescence from cancer cells rises substantially. This has an emission peak at 450–460 nm and a short lifetime in the sub-nanosecond range (~0.5 ns in free form) and larger than 1 ns in bound form. Therefore, the decrease in fluorescence intensity and lifetime for tumor tissue found in this work is consistent with this biochemical compositional change in tumorous areas. Both changes in biochemical composition and morphology in oral cancer tissue appear to result in the decrease of fluorescence lifetime that was found in this study.

In addition, this work showed that the percentage change in intensity (47.8%) of HNSCC was much larger than the change in lifetime (18.9%), but the *p*-value 0.012 of intensity was much higher than that (0.0009) of lifetime. The relatively weaker significance of intensity from the *p*-value may result from the large diversity induced by the nonuniform illumination and the uneven surface of the oral cavity, as it was difficult to provide an ideal flat illumination with this compact endoscope design. In addition, the tissue imaging faced the challenge of irregular morphology, tissue pigmentation, and contamination by blood. Although the fluorescence intensity was a useful reference for visual inspection, it did not provide a reliable standard for cancer diagnosis in the intraoperative environment. Thus, multiple-dimensional imaging (intensity, wavelength, lifetime, and other parameters) is required to improve the diagnosis accuracy.

Although the current study has demonstrated the potential of FLIM for intraoperative evaluation of oral carcinoma, a more practical clinical implementation of this technique would require overcoming a few experimental challenges. We observed that autofluorescence of tumors within oral cavity is relatively weak. The acquisition of a robust set of FLIM data required relatively long data acquisition time, that is, the acquisition of a full set of FLIM images (30 images at the gating time of 0.5 ns and the integration frame of 128) took 120 s. This slow imaging rate is due to the low repetition rate of the nitrogen laser (30 Hz). An additional time is also required to display the processed image data, which currently takes place off-line. Further system improvements are continuing, including the use of a fiber laser at 355 nm at 1 MHz repetition rate to replace the nitrogen laser. This is expected to significantly reduce the time of data acquisition to less than 20 s. An alternative scanning FLIM approach our group recently reported (Sun et al., 2011*a*, 2011*b*, 2012) also has the potential to offset such limitation. Online display of FLIM images will require further integration of data/image analysis algorithms in the FLIM system prototype. Moreover, the ability of the FLIM instrument to accurately diagnose and delineate tumor from surrounding normal tissue during surgical interventions will require generation of a comprehensive database of FLIM features validated by histopathology. This current study was conducted in a limited number of patients and from a few sites in the oral cavity. For a more complete evaluation of FLIM potential for diagnosis of head and neck cancer at distinct stages and at various locations, more patients will need to be included in FLIM intraoperative studies.

Conclusion

This study has demonstrated the application of a wide-field time-domain FLIM endoscopic probe for intraoperative image-guided cancer demarcation. This FLIM apparatus has been designed and developed for clinical studies with a compact portable configuration on a mobile cart. The fiber-optic endoscope has enabled flexible remote access to patients during surgery. Both intensities and time-resolved fluorescence images were successfully collected from the oral cavity. A total of 26 sites from ten patients were evaluated for carcinoma delineation during head and neck surgery. It was found that excitation with a 337-nm laser and tissue autofluorescence in the sub-band of 460/50 nm provided sufficient information for HNSCC differentiation. The average fluorescence lifetime of HNSCC was short lasting ($p < 0.001$) when compared with that of tumor tissue. The fluorescence intensity decreased ($p < 0.05$) in diseased tissue compared with the surrounding normal tissue. Thus, both the fluorescence intensity and lifetime play a role in the discrimination of tumor from the surrounding healthy tissue. However, the differentiation based on time-resolved images was more significant with lower *p*-values, possibly because of robustness from irregular tissue surface, the nonuniform illumination, and the presence of endogenous absorbers. This work demonstrates the potential of FLIM as an intraoperative diagnostic technique based on tissue autofluorescence and guidance of HNSCC surgical resection.

Acknowledgments

This work was supported in part by the National Institutes of Health (Grants R01-HL67377, R21-EB003628, and UL1-RR024146), and the Cancer Center at UC Davis. The authors would like to thank Dough Stephens and Yang Sun for their stimulating discussion and technical help, and Florentine Rutaganira for data processing.

References

Andersson-Engels S, Berg R, Persson A, Svanberg S. Multispectral tissue characterization with time-resolved detection of diffusely scattered white-light. Opt Lett. 1993; 18:1697–1699. [PubMed: 19823488]

Andersson-Engels S, Johansson J, Stenram U, Svanberg K, Svanberg S. Malignant tumour and atherosclerotic plaque diagnosis using laser induced fluorescence. IEEE J Quantum Electron. 1990; 26:2207–2217.

Cubeddu R, Comelli D, D'Andrea C, Taroni P, Valentini G. Time-resolved fluorescence imaging in biology and medicine. J Phys D-Appl Phys. 2002; 35:R61–R76.

De Veld DCG, Witjes MJH, Sterenborg H, Roodenburg JLN. The status of *in vivo* autofluorescence spectroscopy and imaging for oral oncology. Oral Oncol. 2005; 41:117–131. [PubMed: 15695112]

Elson DS, Jo JA, Marcu L. Miniaturized side-viewing imaging probe for fluorescence lifetime imaging (FLIM): Validation with fluorescence dyes, tissue structural proteins and tissue specimens. New J Phys. 2007; 9:127.

Elson D, Requejo-Isidro J, Munro I, Reavell F, Siegel J, Suhling K, Tadrous P, Benninger R, Lanigan P, McGinty J, Talbot C, Treanor B, Webb S, Sandison A, Wallace A, Davis D, Lever J, Neil M, Phillips D, Stamp G, French P. Time-domain fluorescence lifetime imaging applied to biological tissue. Photoch Photobio Sci. 2004; 3:795–801.

Jo JA, Fang Q, Papaioannou T, Baker JD, Dorafshar AH, Reil T, Qiao JH, Fishbein MC, Freischlag JA, Marcu L. Laguerre-based method for analysis of time-resolved fluorescence data: Application to *in-vivo* characterization and diagnosis of atherosclerotic lesions. J Biomed Opt. 2006; 11:021004. [PubMed: 16674179]

Lakowicz, JR. Principles of Fluorescence Spectroscopy. 3. New York: Kluwer Academic/Plenum Publishers; 2006.

Liu J, Sun Y, Qi JY, Marcu L. A novel method for fast and robust estimation of fluorescence decay dynamics using constrained least-squares deconvolution with Laguerre expansion. Phys Med Biol. 2012; 57:843–865. [PubMed: 22290334]

Marcu L. Fluorescence lifetime techniques in medical applications. Ann Biomed Eng. 2012; 40:304–331. [PubMed: 22273730]

Marcu L, Jo JA, Fang Q, Papaioannou T, Reil T, Qiao JH, Baker JD, Freischlag JA, Fishbein MC. Detection of rupture-prone atherosclerotic plaques by time-resolved laser-induced fluorescence spectroscopy. Atherosclerosis. 2009; 204:156–164. [PubMed: 18926540]

Pavlova I, Weber CR, Schwarz RA, Williams MD, Gillenwater AM, Richards-Kortum R. Fluorescence spectroscopy of oral tissue: Monte Carlo modeling with site-specific tissue properties. J Biomed Opt. 2009; 14:014009. [PubMed: 19256697]

Phipps J, Sun Y, Saroufeem R, Hatami N, Fishbein MC, Marcu L. Fluorescence lifetime imaging for the characterization of the biochemical composition of atherosclerotic plaques. J Biomed Opt. 2011; 16:096018. [PubMed: 21950932]

Ramanujam, N. Fluorescence spectroscopy *in vivo*. In: Meyers, RA., editor. Encyclopedia of Analytical Chemistry. Chichester: John Wiley and Sons Ltd; 2000. p. 20-56.

Richards-Kortum R, Mitchell MF, Ramanujam N, Mahadevan A, Thomsen S. *In vivo* fluorescence spectroscopy: Potential for non-invasive, automated diagnosis of cervical intraepithelial neoplasia and use as a surrogate endpoint biomarker. J Cell Biochem Suppl. 1994; 19:111–119. [PubMed: 7823582]

Richards-Kortum R, Sevick-Muraca EM. Quantitative optical spectroscopy for tissue diagnosis. Annu Rev Phys Chem. 1996; 47:555–606. [PubMed: 8930102]

Schwarz RA, Gao W, Weber CR, Kurachi C, Lee JJ, EL-Naggar AK, Richards-Kortum R, Gillenwater AM. Noninvasive evaluation of oral lesions using depth-sensitive optical spectroscopy. Cancer. 2009; 115:1669–1679. [PubMed: 19170229]

Skala MC, Riching KM, Gendron-Fitzpatrick A, Eickhoff J, Eliceiri KW, White JG, Ramanujam N. *In vivo* multiphoton microscopy of NADH and FAD redox states, fluorescence lifetimes, and cellular morphology in precancerous epithelia. Proc Natl Acad Sci USA. 2007; 104:19494–19499. [PubMed: 18042710]

Sun Y, Chaudhari AJ, Lam M, Xie H, Yankelevich DR, Phipps J, Liu J, Fishbein MC, Cannata JM, Shung KK, Marcu L. Multimodal characterization of compositional, structural and functional features of human atherosclerotic plaques. Biomed Opt Express. 2011a; 2:2288–2298. [PubMed: 21833365]

Sun Y, Phipps J, Elson DS, Stoy H, Tinling S, Meier J, Poirier B, Chuang FS, Farwell DG, Marcu L. Fluorescence lifetime imaging microscopy: *In vivo* application to diagnosis of oral carcinoma. Opt Lett. 2009; 34:2081–2083. [PubMed: 19572006]

Sun Y, Sun Y, Stephens D, Xie H, Phipps J, Saroufeem R, Southard J, Elson DS, Marcu L. Dynamic tissue analysis using time- and wavelength-resolved fluorescence spectroscopy for atherosclerosis diagnosis. Opt Express. 2011b; 19:3890–3901. [PubMed: 21369214]

Sun Y, Xie HT, Liu J, Lam M, Chaudhari AJ, Zhou FF, Bec J, Yankelevich DR, Dobbie A, Tinling SL, Gandour-Edwards RF, Monsky WL, Farwell DG, Marcu L. *In vivo* validation of a bimodal technique combining time-resolved fluorescence spectroscopy and ultrasonic backscatter microscopy for diagnosis of oral carcinoma. J Biomed Opt. 2012; 17:116003. [PubMed: 23117798]

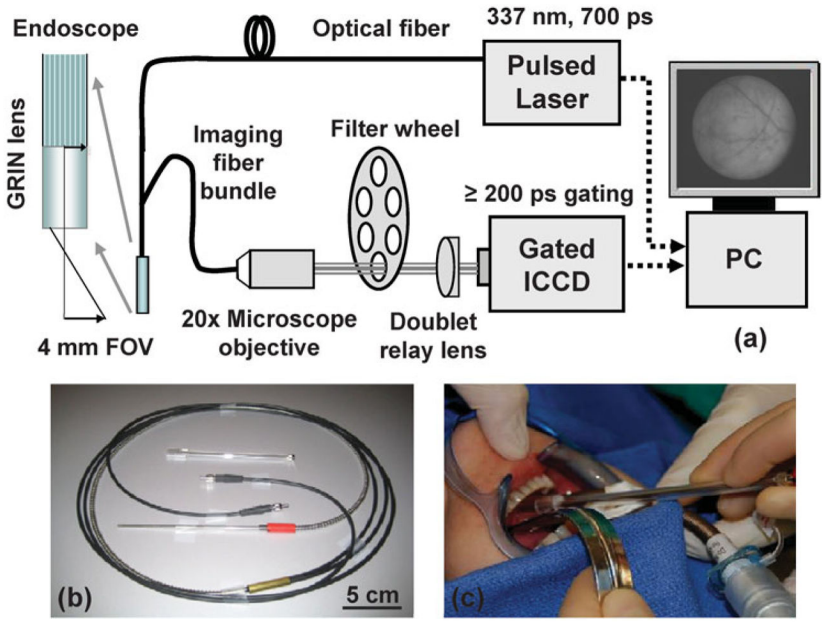

Figure 1.

Fluorescence lifetime imaging microscopy (FLIM) system for intraoperative diagnosis of oral carcinoma. **a:** Endoscopic FLIM schematic. **b:** Picture of the semiflexible integrated endoscope used in patients studies. **c:** Picture of the FLIM probe applied to oral cavity.

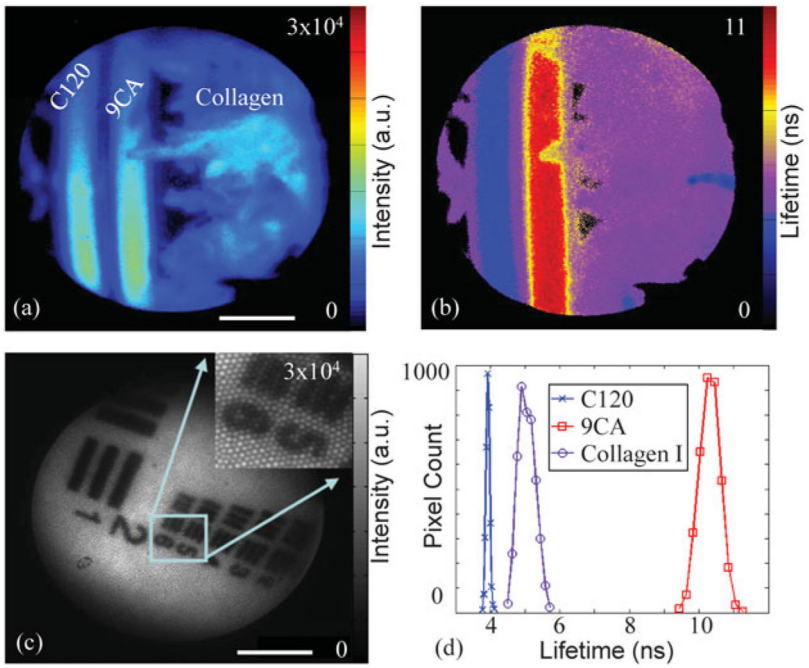

Figure 2.

Performance evaluation of fluorescence lifetime imaging microscopy system using fluorophores and biomolecules: (**a**) fluorescence intensity images and (**b**) average lifetime images of the coumarin 120 (C120), and 9-cyanoanthracene (9CA) dye solutions in capillaries placed on top of a dry collagen bed. Images acquired using the 460/50 nm filter. **c:** Image resolution was evaluated using a USAF test chart at a 0.2 ns gating time. Scale bar is 1 mm. **d:** Fluorescence lifetime histograms of the C120, 9CA, and collagen corresponding to images in (**b**).

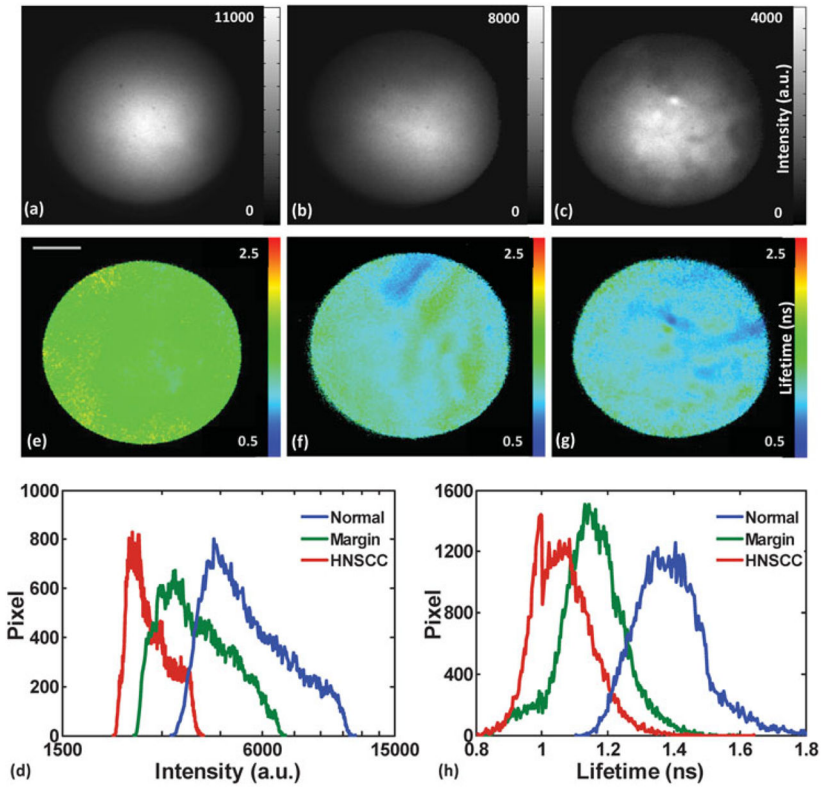

Figure 3.

Autofluorescence fluorescence lifetime imaging microscopy images of human buccal mucosa: (**a**)–(**c**) depict the intensity images, and (**e**)–(**g**) depict the average lifetime images from three areas: normal, tumor, and adjacent normal-tumor, their corresponding histograms are depicted in (**d**) for intensity and (**h**) for average lifetime. HNSCC, head and neck squamous cell carcinoma.

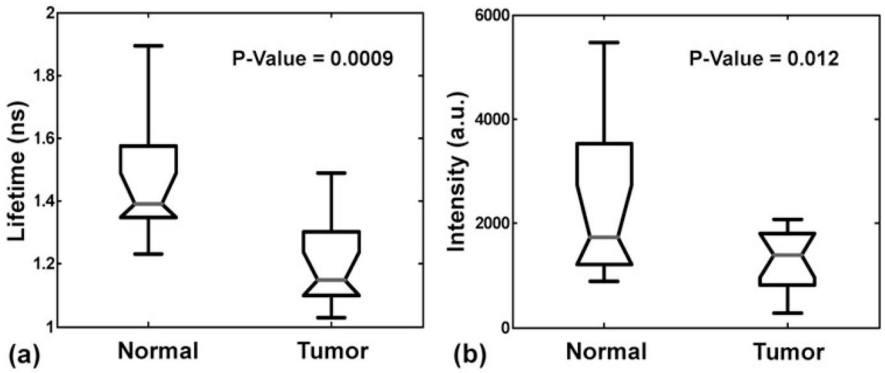

Figure 4.

Statistical analysis (analysis of variance) for (**a**) average lifetime values and (**b**) intensity values depicting the difference between two groups of data. The data from all 26 sites were included in the analysis.

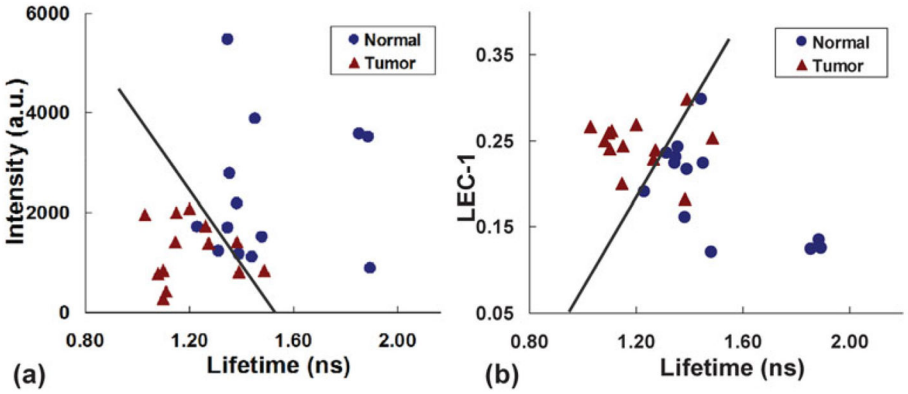

Figure 5.

Scatter plots depicting the ability of distinct fluorescence-derived parameters to differentiate between tumor and normal tissue: (**a**) intensity versus lifetime; (**b**) Laguerre coefficients (LEC)-1 versus lifetime.

Table 1

Summary of Average Lifetime, Intensity, and Laguerre Coefficients (LECs) from Head and Neck Tumor Experiments.

	Lifetime (ns)	Intensity (AU)	LEC-0	LEC-1	LEC-2	LEC-3
Normal	1.49 ±0.06[a]	2,365 ±382	0.43 ±0.06	0.19 ±0.06	−0.11 ±0.04	0.23 ±0.02
Tumor	1.21 ±0.04	1,233 ±168	0.23 ±0.04	0.25 ±0.01	−0.22 ±0.04	0.28 ±0.01
P-value	0.0009	0.012	0.016	0.008	0.060	0.040

[a]Standard error